

1      **Estimating the impact of a major hurricane on**  
2      **transport processes**

3      Thomas Dobbelaere, Emmanuel Hanert

4      February 16, 2021

5      **Abstract**

6      In most hydrodynamic model studies, currents and waves are simu-  
7      lated separately. This is especially true for the simulation of passive  
8      drifters, whose trajectories are often computed based solely on cur-  
9      rents. Although this simplification holds for most situations, as the  
10     force exerted by waves on currents can be neglected in fair weather  
11     conditions, it may lead to significant errors in storm conditions, during  
12     which local currents are strongly influenced by wind-generated waves.  
13     In this study, current-wave interactions in heavy-wind conditions are  
14     studied by coupling the unstructured-mesh hydrodynamic model SLIM  
15     with the wave model SWAN in the Florida Reef Tract during Hurricane  
16     Irma (Sep. 2017). This coupled model successfully reproduced both  
17     the observed wave behavior and storm surge during the hurricane.  
18     The modeled currents were then used to simulate the trajectories of  
19     passive drifters during the passage of the hurricane. Our results show  
20     that taking wave force into account induces variations of up 1 m/s in  
21     modelled currents on the continental shelf break as well as in the vicin-  
22     ity of reefs and islands. Wave-current interactions can therefore deflect  
23     the trajectories of drifting material by up to 10 km during heavy-wind  
24     events. These results strongly advocate for the inclusion of wave forces  
25     while studying transport processes (sediments, pollutants, larvae, etc.)  
26     under storm conditions

27    **1 Introduction**

28    Wave-current interactions in coastal areas are of great importance for coastal  
29    engineering as they play a key role in sediment transport, morphological  
30    evolution and pollutant mixing (Bever and MacWilliams, 2013; Li and Johns,  
31    1998). However, these interactions are highly nonlinear and can vary sig-  
32    nificantly in space and time (Wu et al., 2011). Wave-induced currents are  
33    generated by wave radiation gradients (Longuet-Higgins, 1970), affecting  
34    water levels near shorelines and wave breaking points (Longuet-Higgins  
35    and Stewart, 1964), while changes in water levels and currents, in turn,  
36    affect the motion and evolution of waves (Sikirić et al., 2013). Coupled  
37    wave-current models are therefore required to capture these complex inter-  
38    actions. As coastal oceans are characterized by local complex geometries  
39    with islands, inlets and estuaries, unstructured (usually two-dimensional)  
40    models are preferred as structured grid models show limitations in resolving  
41    topologically controlled nearshore processes (Wu et al., 2011; Chen et al.,  
42    2007). The effect of wave-interactions becomes even more significant in  
43    the case of hurricanes, that generate large wind-waves and disturb ocean  
44    conditions (Liu et al., 2020) by causing coastal upwellings on continental  
45    shelves (Smith, 1982) and inducing strong currents, waves and storm surges  
46    in nearshore and coastal regions (Dietrich et al., 2010; Weisberg and Zheng,  
47    2006). South Florida and the Gulf of Mexico are particularly vulnerable to  
48    hurricanes (Malmstadt et al., 2009) and modelling studies predict tropical  
49    cyclones to increase both in frequency and intensity in this region (Mar-  
50    sooli et al., 2019; Knutson et al., 2010). Being able to accurately model  
51    wave-current interactions in this area becomes thus critical.

52    Individual-based modelling of particulates has been extensively used to  
53    study the transport of drifting materials such as pollutants, sediments or  
54    larvae (Garcia-Pineda et al., 2020; Liubartseva et al., 2018; Figueiredo et al.,  
55    2013; Frys et al., 2020). Although some of these studies take the impact  
56    of waves into account by adding Stokes drift velocity, *i.e.* the net drift of a  
57    floating particle in the direction of the wave propagation (Van Den Bremer  
58    and Breivik, 2018), to the Eulerian currents, they usually neglect the wave-  
59    induced currents. Such practice is reasonable in the case of fair weather,  
60    when wave-induced forces exerted on currents are relatively smaller, but  
61    might lead to significant inaccuracies during storm conditions. To assess

62 the importance of wave-current interactions during a tropical cyclone, we  
63 investigated the transport of drifting particulates on the Florida shelf during  
64 Hurricane Irma, one of the strongest and costliest tropical cyclones on  
65 records in the Atlantic Basin (Chen et al., 2007), that made landfall in Florida  
66 in September 2017.

67 In this study, we developed an unstructured coupled wave-current model of  
68 South Florida to simulate the ocean circulation during hurricane Irma. Both  
69 modelled currents and waves were validated against field measurements  
70 and were then used to simulate the transport of drifting particulates in the  
71 Florida Keys and the Florida inner shelf during the storm. Model outputs  
72 were then compared with uncoupled simulation results in order to assess  
73 the impact of wave-induced forces and Stokes drift on the modelled currents  
74 and transports.

## 75 **2 Methods**

### 76 **2.1 Study area and data**

77 Large-scale ocean circulation around South Florida is dominated by the  
78 Florida Current (FC), which originates from the Loop Currents (LC) where it  
79 enters the Florida Straits from the Gulf of Mexico, and, downstream, forms  
80 the Gulf Stream. The FC is a major western boundary current character-  
81 ized by spatial variability and meandering, associated with the presence  
82 of cyclonic eddies between the core of the current and the complex reef  
83 topography of the Florida Reef Tract (FRT) (Frys et al., 2020; Lee et al.,  
84 1995; Kourafalou and Kang, 2012). The northern half of these reefs are  
85 made of early Holocene reef frameworks and indurated sand ridges while  
86 the southern part (the Florida Keys) is composed of a chain of limestone is-  
87 lands, fossilized remnants of ancient coral reefs and sand bars (Hoffmeister  
88 and Multer, 1968; Shinn, 1988; Lidz and Shinn, 1991). The variability of the  
89 FC extends over a large range of spatial and temporal scales, with periods  
90 of 30-70 days in the Lower Keys (Lee et al., 1995) and shorter periods of  
91 2-21 days in the Upper Keys (Lee and Mayer, 1977), and exhibits significant  
92 seasonal and interannual cycles (Johns and Schott, 1987; Lee and Williams,  
93 1988; Schott et al., 1988). Circulation on the West Florida Shelf (WFS) on

94 the other hand is forced by local winds and tidal fluctuations (Lee and Smith,  
95 2002; Liu and Weisberg, 2012).

96 Field observations were used to validate our model outputs. Modelled sea  
97 surface elevation was validated against tide gauge measurements from  
98 the National Oceanic and Atmospheric Administrations (NOAA) Tides and  
99 Currents dataset. These measurements were taken at four locations: two  
100 in the Florida Keys (Key West and Vaca Key); one on the eastern coast  
101 of Florida (Key West); and one on the western coast (Naples). Currents  
102 were validated against ADCP measurements from the University of South  
103 Florida's College of Marine Science's (USF/CMS) Coastal Ocean Monitoring  
104 and Prediction System (COMPS) for the WFS (Weisberg et al., 2009). More  
105 specifically, we used measurements from moorings C10, C12 and C13,  
106 respectively located at the 25, 50, and 50 m isobaths of the WFS (Liu  
107 et al., 2020). Finally, validation of modelled wave parameters was performed  
108 against four buoy measurements from NOAA's National Data Buoy Center  
109 (NDBC): two on Florida's Eastern shelf and two on the WFS. The locations  
110 of all measurement stations are shown on Fig. 1

## 111 **2.2 Wind and atmospheric pressure for Hurricane Irma**

112 Irma made landfall in Florida on 10 September 2017 as a category 3 storm,  
113 first at Cudjoe Key (Florida Keys) and later on Marco Island, south to Naples  
114 (see Fig. 1). It then weakened to a category 2 storm as it moved further  
115 inland (Pinelli et al., 2018). The storm caused damages to up to 75% of  
116 the buildings at his landfall point in the Florida Keys, making it one of the  
117 strongest and costliest hurricanes on record in the Atlantic basin (Xian  
118 et al., 2018; Zhang et al., 2019). The strongest reported wind speed was  
119 50 m/s on Marco Island while the highest recorded storm surge was 2.3  
120 m, although larger wind speed likely occurred in the Florida Keys (Pinelli  
121 et al., 2018) In order to reproduce the wind profile of Irma in our model,  
122 high-resolution H\*Wind (Powell et al., 1998) wind fields were used. As  
123 these data represent 1-min averaged wind speeds, we multiplied them by  
124 a factor 0.93 to obtain 10-min averaged wind speeds (Harper et al., 2010),  
125 more consistent with the time step of our model. Furthermore, H\*Wind  
126 wind profiles did not cover the whole model extent during the hurricane and

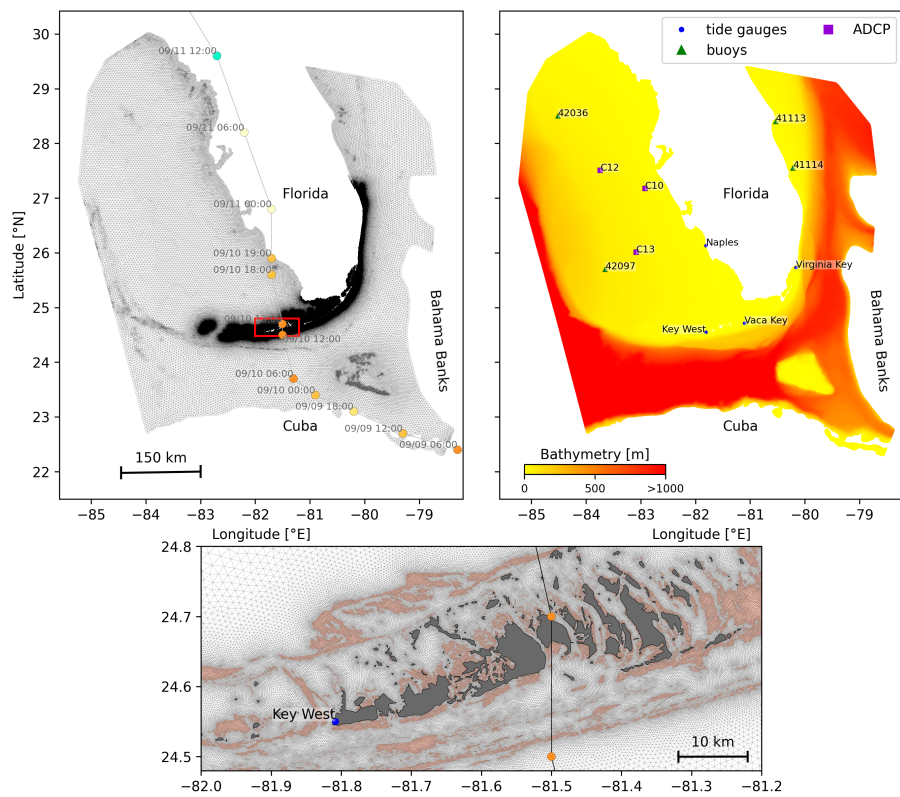


**Fig. 1:** Upper left: Mesh of the computational domain with the trajectory of Irma, category of the hurricane is given by the Saffir-Simpson color scale. Upper right: Bathymetry of the domain with the location of stations used for the validation of the model outputs. Lower center: Close up view of the 100m mesh resolution near reefs and islands; islands are highlighted in dark grey and coral reefs in coral

127 were thus blended within coarser wind field extracted from ECMWF ERA-5  
 128 datasets. Pressure fields of Irma were also constructed using ERA-5 data.  
 129 However, the coarse resolution of the data set caused the depression at the  
 130 center of the hurricane to get smoothed out, leading to an underestimation  
 131 of the pressure gradient in our model (see eq. 1). To better capture the  
 132 central depression of Irma, we built a hybrid pressure field using the position  
 133 and the minimal pressure of the core of the hurricane based on its track  
 134 in the HURDAT 2 database (Landsea and Franklin, 2013). Based on this  
 135 information, the hybrid pressure field was constructed by combining an  
 136 idealized Holland pressure profile (Lin and Chavas, 2012) within the radius  
 137 of maximum wind speed of Irma (Knaff et al., 2018) with ERA-5 pressure  
 138 field. The transition between from the Holland profile to ECMWF data outside  
 139 the radius of maximum wind speed data was performed using a smooth step  
 140 function.

### 141 **2.3 Hydrodynamic model**

142 Ocean currents generated during hurricane Irma around South Florida  
 143 were modelled using the unstructured-mesh depth-integrated coast ocean  
 144 model SLIM<sup>1</sup>. The model mesh covers an area similar to the model extent  
 145 of Dobbelaere et al. (2020b), that includes the FRT but also the Florida  
 146 Strait and part of the Gulf of Mexico (Figure 1). However, this area has  
 147 been slightly extended northeastward and westward in order to include  
 148 the location of buoys for wave outputs validation. Furthermore, in order to  
 149 withstand potential cell drying due to storm conditions in this study, we used  
 150 the conservative mode of SLIM with wetting-drying, whose equations write:

$$\begin{aligned}
 \frac{\partial H}{\partial t} + \nabla \cdot (\mathbf{U}) &= 0 \\
 \frac{\partial \mathbf{U}}{\partial t} + \nabla \cdot \left( \frac{\mathbf{U}\mathbf{U}}{H} \right) &= -f \mathbf{e}_z \times \mathbf{U} + \alpha g H \nabla(H - h) - \frac{1}{\rho} \nabla p_{\text{atm}} + \frac{1}{\rho} \boldsymbol{\tau}_s \quad (1) \\
 &\quad + \nabla \cdot (\nu \nabla \mathbf{U}) - \frac{C_b}{H^2} |\mathbf{U}| \mathbf{U} + \gamma (\mathbf{U}_* - \mathbf{U})
 \end{aligned}$$

151 where  $H$  is the water column height and  $\mathbf{U}$  is the depth-averaged transport;  
 152  $f$  is the Coriolis coefficient;  $g$  is the gravitational acceleration;  $h$  is the

---

<sup>1</sup><https://www.slim-ocean.be>

153 bathymetry;  $\alpha$  is a coefficient stating whether the mesh element is wet  
 154 ( $\alpha = 1$ ) or dry ( $\alpha = 0$ );  $\nu$  is the viscosity;  $C_b$  is the bottom drag coefficient;  
 155  $\nabla p_{\text{atm}}$  is the atmospheric pressure gradient;  $\tau_s$  is the surface stress due  
 156 to wind; and  $\gamma$  is a relaxation coefficient towards a reference transport  $\mathbf{U}_*$ .  
 157 As in Frys et al. (2020) and Dobbelaere et al. (2020b), SLIM currents were  
 158 relaxed towards HYCOM (Chassignet et al., 2007) in regions where the water  
 159 depth exceeds a given threshold. At very high wind speeds, the white cap is  
 160 blown off the crest of the waves, which generates a layer of droplets that acts  
 161 as a slip layer for the winds at the ocean-atmosphere interface (Holthuijsen  
 162 et al., 2012). This causes a saturation of the wind drag coefficient for strong  
 163 winds (Donelan et al., 2004; Powell et al., 2003). To account for the impact  
 164 of this saturation on the surface wind stress in our model, we implemented  
 165 the wind drag parameterization of Moon et al. (2007).  
 166 The mesh resolution depended on the distance to coastlines and reefs,  
 167 bathymetry and bathymetry gradient in order to satisfy SWAN refinement  
 168 criterion  $h/A \geq a$ , where  $h$  is the water depth and  $A$  is the element area.  
 169 The mesh was generated using the Python library seamsh<sup>2</sup>, based on the  
 170 the open-source mesh generator GMSH (Geuzaine and Remacle, 2009) and  
 171 is composed of approximately  $7.7 \times 10^5$  elements. The coarsest elements,  
 172 far away from the FRT, had a characteristic length size of about 5 km, as  
 173 shown in Fig 1 along with the bathymetry of the model domain.

## 174 2.4 Wave model

175 Waves were modelled using parallel unstructured SWAN (Booij et al., 1999)  
 176 on the same mesh as SLIM. This model solves the action balance equation,  
 177 which reads (Mei, 1989):

$$\frac{\partial N}{\partial t} + \nabla_{\mathbf{x}} \cdot [(\mathbf{c}_g + \mathbf{u})N] + \frac{\partial}{\partial \theta}[c_\theta N] + \frac{\partial}{\partial \sigma}[c_\sigma N] = \frac{S_{in} + S_{ds} + S_{nl}}{\sigma} \quad (2)$$

178 where  $N = E/\sigma$  is the wave action density;  $\theta$  is the wave propagation direc-  
 179 tion;  $\sigma$  is the wave relative frequency;  $\mathbf{c}_g$  is the wave group velocity,  $\mathbf{u}$  is SLIM  
 180 depth-averaged current velocity;  $c_\theta$  and  $c_\sigma$  are the propagation velocities in  
 181 spectral space due to refraction and shifting in frequency due to variations

---

<sup>2</sup><https://pypi.org/project/seamsh/>

182 in depth and currents; and  $S_{in}$ ,  $S_{ds}$ , and  $S_{nl}$  respectively represent wave  
 183 growth by wind, wave decay and nonlinear transfers of wave energy through  
 184 interactions between triplets and quadruplets. Spectra were discretized with  
 185 48 direction bins and 50 frequency bins logarithmically distributed from 0.3 to  
 186 2 Hz. Exponential wind growth was parameterized using the formulation of  
 187 Janssen (1991), while dissipations by whitecapping and bottom dissipations  
 188 followed the formulations of Komen et al. (1984) and Madsen et al. (1989)  
 189 respectively. Coefficients for exponential wind growth and whitecapping  
 190 parameterizations were based on the results of Siadatmousavi et al. (2011).  
 191 Finally, wave boundary conditions were derived from WAVEWATCH III (Tol-  
 192 man et al., 2009) spectral outputs at buoy locations. Depth-averaged Stokes  
 193 drift was also computed by SWAN using the following formula:

$$\mathbf{u}_s = \int_0^{2\pi} \int_0^{+\infty} \frac{\sigma^3}{h \tanh(2kh)} E(\sigma, \theta) (\cos \theta, \sin \theta) d\sigma d\theta \quad (3)$$

194 where  $k$  is the norm of the wave vector;  $h$  is the water depth; and  $E(\sigma, \theta)$  is  
 195 the wave energy density.

## 196 2.5 Coupled model

197 The coupling between SLIM and SWAN is illustrated in Figure 2. The two  
 198 models are run consecutively at each time step. First, SLIM computes the  
 199 sea surface elevation  $\eta$  and depth-averaged current velocity  $\mathbf{u} = (u, v)$ .  
 200 These quantities are transferred to SWAN to update the model water depth  
 201 as well as the second term of equation 2 governing wave energy propagation  
 202 in the geographic space. Moreover, in order for the two model to have con-  
 203 sistent bottom dissipation parameterizations, SLIM bottom drag coefficient is  
 204 transformed into a roughness length  $z_0$  following the methodology of Dietrich  
 205 et al. (2011). This roughness length is then converted into Madsen's bottom  
 206 dissipation term in SWAN. SWAN then produces the wave-induced force on  
 207 current  $\tau_{wave}$  by computing the wave radiation stress gradient. This quantity  
 208 is used to update the value of the surface stress  $\tau_s$  in equation 1, that now  
 209 becomes the sum of wind and wave-induced forces  $\tau_s = \tau_{wind} + \tau_{wave}$ .

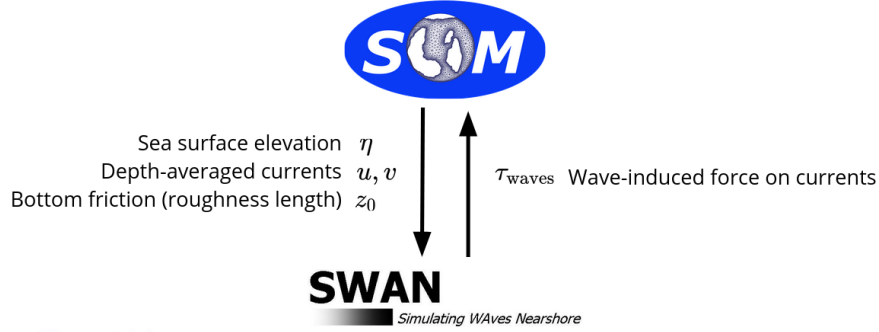


**Fig. 2:** Schematic illustration of the coupled SLIM+SWAN model.

## 210 2.6 Comparison of particle trajectories

211 To assess the impact of the wave coupling on the modelled currents during  
 212 hurricane Irma, we compared the trajectories of virtual particles driven  
 213 by currents produced by SLIM alone and SLIM+SWAN simulations in the  
 214 Florida Keys. First, we identified the areas where the differences between  
 215 the modelled currents were the largest. Then, we determined the potential  
 216 origination regions of particles reaching these areas on the passage of the  
 217 hurricane through the Florida Keys using backtracking methods (Dobbelaeere  
 218 et al., 2020a). These regions are highlighted by the 4 release regions of Fig.  
 219 7. Finally, particles were released from these four regions and advected by  
 220 currents produced by the coupled and uncoupled models. At each time step,  
 221 the center of mass of the modelled particle clouds were computed. The dis-  
 222 tance between these centers of mass was used as a measure of the impact  
 223 of the wind-generated wave coupling on the modelled current in the Florida  
 224 Keys during hurricane Irma. This comparison was performed with 3 sets  
 225 of currents: the currents modelled by uncoupled SLIM (SLIM); the currents  
 226 modelled by coupled SLIM+SWAN (SLIM+SWAN); and the SLIM+SWAN  
 227 currents with depth-averaged Stokes drift (SLIM+SWAN+Stokes).

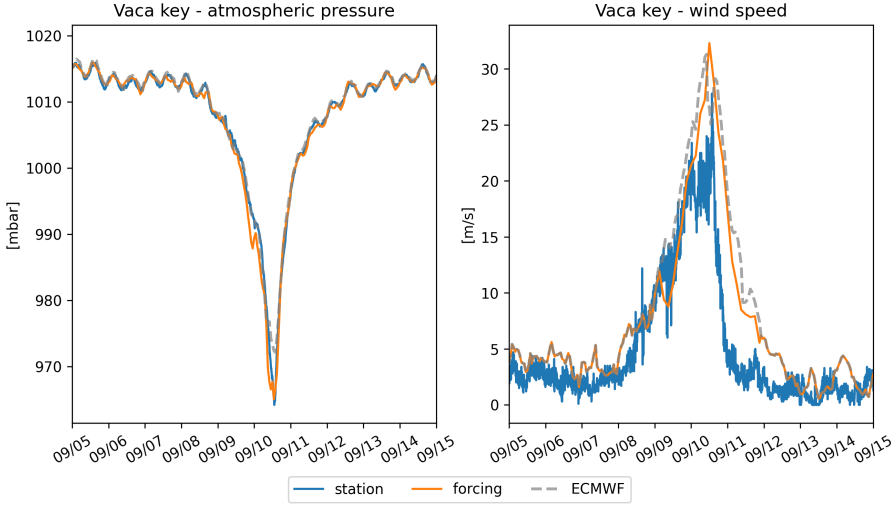


**Fig. 3:** Comparison of reconstructed wind atmospheric pressure with field measurements and coarser ECMWF ERA-5 profiles during Irma. The generated hybrid atmospheric better capture the observed storm depression while H\*wind winds better match the measured peak in wind speed.

### 228 3 Results

#### 229 3.1 Validation

230 Comparisons of H\*Wind wind and hybrid pressure fields with station mea-  
 231 surements and ECMWF ERA-5 profiles at Vaca Key station are shown in Fig.  
 232 3. The hybrid pressure field shows better agreement with observations than  
 233 ERA-5 pressure as it successfully reproduces the storm depression. ERA-5  
 234 fields, on the other hand, fail to resolve the low pressure at the core of the  
 235 hurricane due to their coarser grid. Both H\*Wind and ERA-5 agree well with  
 236 observed wind speeds although both data sets tend to slightly overestimate  
 237 the width and intensity of the wind peak. However, H\*wind profiles show a  
 238 better match with the timing of the observed peak, that ERA-5 winds tend  
 239 to anticipate. H\*wind also exhibits a slightly narrower peak in wind speed,  
 240 which better agrees with observations.

241 Hydrodynamic outputs of the coupled wave-current model were validated  
 242 against tide gauge and ADCP measurements at the stations highlighted  
 243 in Fig. 1. Comparison of modelled and observed sea surface elevation is  
 244 shown in Fig. 4. Timing and intensities of the storm surges are successfully

reproduced by the coupled model, the largest model error being an overestimation of 18 cm of the elevation peak at Virginia Key. The fit is especially good at Naples, where both the positive and negative surges are captured by the coupled model with a 5 cm accuracy. This result is of interest as negative surges, although less studied, affect water exchanges between the estuaries and the coastal ocean and disturb the benthic ecosystems (Liu et al., 2020). Modelled 2d currents were validated against depth-averaged ADCP measurements at mooring station C10, C12 and C13 are also shown in Fig. 4. As in (Liu et al., 2020), vector correlation analysis (Kundu, 1976) is performed to compare modelled and observed current velocity vectors. Correlation coefficients ( $\rho$ ) between simulated and observed depth-averaged currents were 0.84, 0.74 and 0.73 respectively C10, C12 and C13 locations respectively. Average veering angles were computed as well and were below  $12^\circ$ , as in (Liu et al., 2020). However, in our case, no clear overestimation of southward currents was observed during Irma. As expected from a depth-averaged model, the best fit with observations is obtained at the shallowest mooring C10, located on the 25m isobath, with an average veering angle of  $6^\circ$ .

The wave parameters computed by the coupled model were validated against field measurements as well. Validation data was extracted from four buoys, two in the Eastern coast Florida and two in the inner shelf. Results of Fig. 5 show that the model reproduces correctly the timing and amplitude of the significant wave height peak during the hurricane for all four stations. Modelled wave period and direction are in good agreement with measurement as well, as shown for station 42036.

### 3.2 Impact of waves on currents and transport

The impact of hurricane-induced wave-current interactions is first evaluated by computing the norm of the maximal difference in current velocity between uncoupled SLIM and coupled SLIM+SWAN model runs during the passage of Irma through the Florida Keys (from 2017-09-07 to 2017-09-13). Figure 6 shows that differences in modelled currents are stronger on the shelf break and over coral reefs. These results highlight the significant impact of wave-induced forces, that can yield differences of up to 1 m/s during the

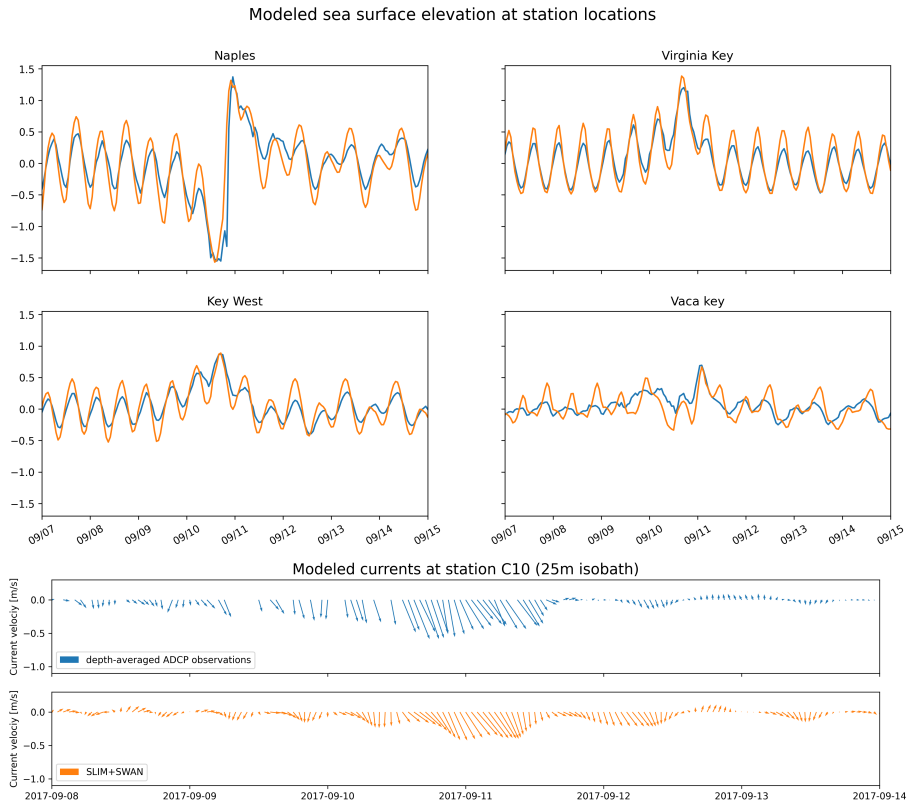


**Fig. 4:** Comparison of modelled sea surface elevation and current velocity with tide gauge measurements and observed velocity at mooring C10. Timing and intensities of the positive and negative storm surges are well reproduced by the model. Modelled current velocities agree well with observations, with a correlation coefficient of 0.83 and an average veering angle of  $6^\circ$  at mooring C10.

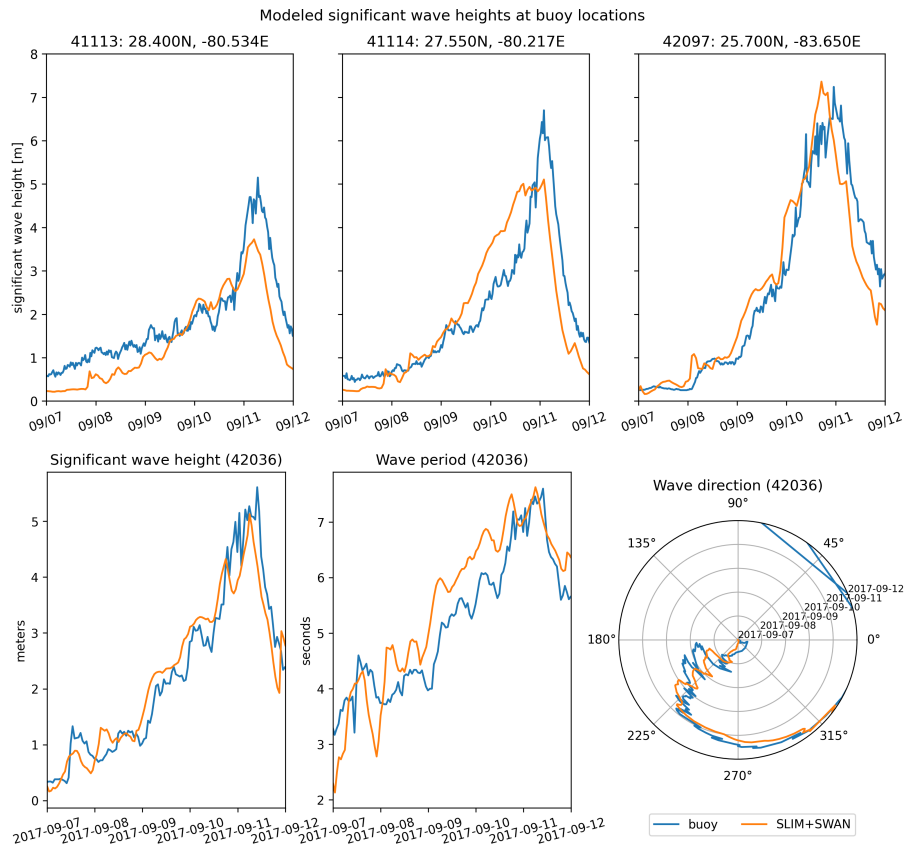


**Fig. 5:** The significant wave height produced by the coupled model has been compared to buoy measurements at 4 different stations. The timing and amplitude of the peak during the hurricane is correctly reproduced for all stations. For station 42036, the period and direction of the waves also agree well with observations

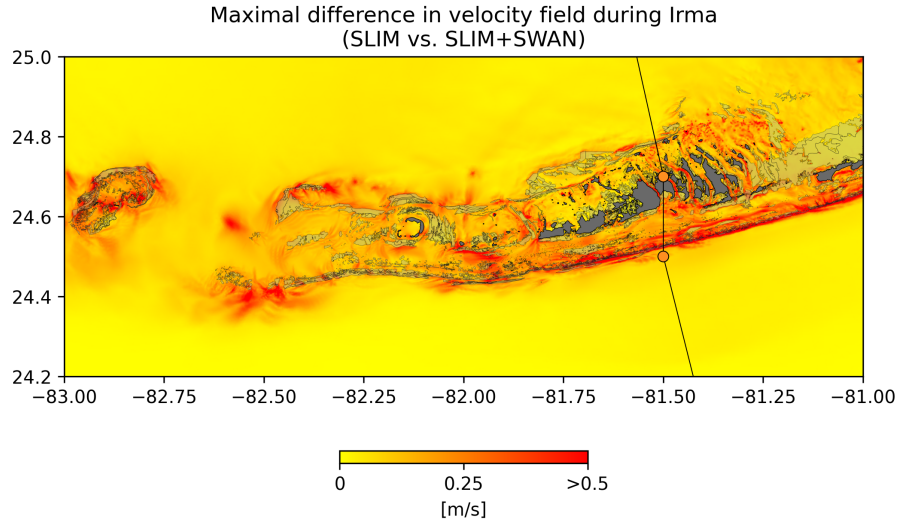


**Fig. 6:** Maximum of the difference between SLIM and SLIM+SWAN currents speed between 2017-09-07 00:00:00 and 2017-09-13 00:00:00. The difference between the coupled and uncoupled model, which represents the effect of the wave-induced stress, can yield differences of 0.5 m/s in the simulated currents during the passage of the hurricane. SLIM+SWAN currents velocities are larger than the currents modeled by SLIM alone. Islands are highlighted in dark grey and coral reefs in lighter grey

278 hurricane, with stronger currents being obtained with SLIM+SWAN. This  
 279 suggests that neglecting wave-current interactions during Irma would result  
 280 in a significant underestimation of transport over reefs.

281 To quantify the impact of these differences in velocity fields on the modelled  
 282 trajectories of passive drifters such as coral larvae, we then tracked virtual  
 283 particles advected by SLIM, SLIM+SWAN and SLIM+SWAN+Stokes cur-  
 284 rents. Comparison of SLIM and SLIM+SWAN+Stokes trajectories are shown  
 285 in Fig. 7. Differences between the modelled trajectories are negligible before  
 286 the passage of the hurricanes in the Florida Keys. Then, distance between  
 287 the centers of mass of the particles abruptly increase to up to tens of kilo-  
 288 meters as Irma gets through the Keys to finally stabilize after the passage  
 289 of the hurricane. These results support the assumption that wave-induced  
 290 transport is negligible compared to advection by Eulerian currents in fair  
 291 whether conditions. However, ignoring waves in storm conditions could  
 292 result in significant inaccuracies in modelled trajectories, as illustrated in  
 293 the case of release region 2 in Fig. 7. Particles advected by the currents

294 of the coupled model tend to remain on the shelf while particles advected  
295 by SLIM alone are mostly transported along the shelf break. Although not  
296 shown in this paper, comparison of SLIM and SLIM+SWAN trajectories were  
297 conducted as well. The evolution of the distance between centers of mass  
298 of the particle clouds showed similar trends while yielding smaller values.  
299 Modelled maximal depth-averaged Stokes drift reached up to 0.2 m/s during  
300 the passage of Irma through the Florida Keys. This suggests that both the  
301 impact of wave-induced force on Eulerian currents and Stokes drift should be  
302 taken into account while modelling particle transport under storm conditions.

## 303 **4 Discussion and conclusions**

304 Impact of waves on coral connectivity

305 Ability of wave model to correctly capture gradient in significant wave height  
306 due to current-waves interactions under tropical cyclones depends on:

- 307 • Spatial (10km → 5km) and spectral (36 dir. → 48 dir.) resolution  
308 (Hegermiller et al., 2019)
- 309 • Directional spreading of incident waves (Villas Bôas et al., 2020)

## 310 **Conflict of Interest Statement**

311 The authors declare that the research was conducted in the absence of any  
312 commercial or financial relationships that could be construed as a potential  
313 conflict of interest.

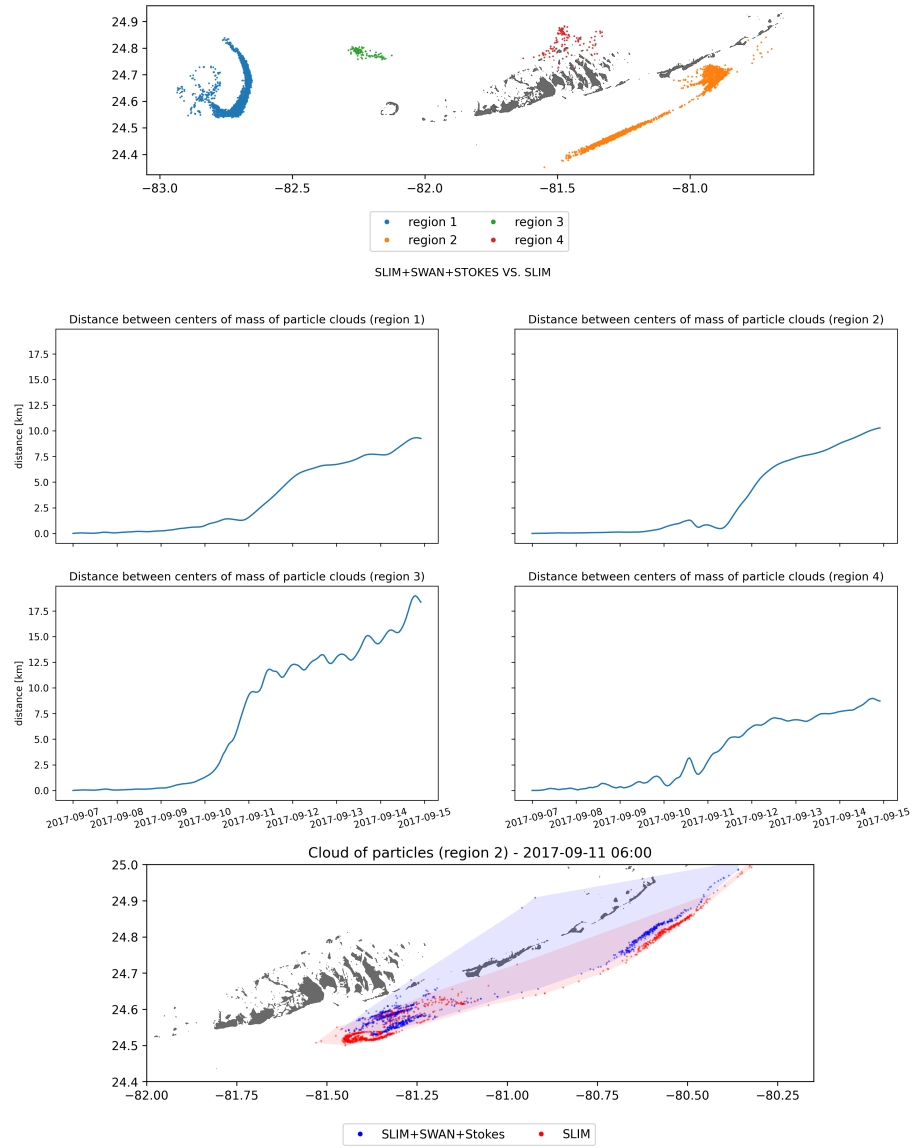


**Fig. 7:** Comparison of passive drifters trajectories with SLIM+SWAN+Stokes drift vs. SLIM alone. A snapshot of the positions of the particles released from region 2 is shown after the passage of Irma in the Florida Keys. Particles advected by the currents of the coupled model tend to remain on the shelf while particles advected by SLIM alone are mostly transported along the shelf break

<sup>314</sup> **Author Contributions**

<sup>315</sup> **Funding**

<sup>316</sup> **Acknowledgments**

<sup>317</sup> Computational resources were provided by the Consortium des Équipements  
<sup>318</sup> de Calcul Intensif (CÉCI), funded by the F.R.S.-FNRS under Grant No. 2.5020.11.  
<sup>319</sup> Thomas Dobbelaere is a PhD student supported by the Fund for Research  
<sup>320</sup> training in Industry and Agriculture (FRIA/FNRS).

<sup>321</sup> **Supplementary Material**

<sup>322</sup> The Supplementary Material for this article is attached to the submitted  
<sup>323</sup> document.

<sup>324</sup> **References**

- <sup>325</sup> Bever, A. J. and MacWilliams, M. L. (2013). Simulating sediment transport  
<sup>326</sup> processes in San Pablo Bay using coupled hydrodynamic, wave, and  
<sup>327</sup> sediment transport models. *Marine Geology*, 345:235–253.
- <sup>328</sup> Booij, N., Ris, R. C., and Holthuijsen, L. H. (1999). A third-generation wave  
<sup>329</sup> model for coastal regions: 1. Model description and validation. *Journal*  
<sup>330</sup> *of geophysical research: Oceans*, 104(C4):7649–7666.
- <sup>331</sup> Chassignet, E. P., Hurlbert, H. E., Smedstad, O. M., Halliwell, G. R., Hogan,  
<sup>332</sup> P. J., Wallcraft, A. J., Baraille, R., and Bleck, R. (2007). The HYCOM  
<sup>333</sup> (hybrid coordinate ocean model) data assimilative system. *Journal of*  
<sup>334</sup> *Marine Systems*, 65(1-4):60–83.
- <sup>335</sup> Chen, C., Huang, H., Beardsley, R. C., Liu, H., Xu, Q., and Cowles, G. (2007).  
<sup>336</sup> A finite volume numerical approach for coastal ocean circulation studies:  
<sup>337</sup> Comparisons with finite difference models. *Journal of Geophysical*  
<sup>338</sup> *Research: Oceans*, 112(C3).

- 339 Dietrich, J., Bunya, S., Westerink, J., Ebersole, B., Smith, J., Atkinson,  
340 J., Jensen, R., Resio, D., Luettich, R., Dawson, C., et al. (2010). A  
341 high-resolution coupled riverine flow, tide, wind, wind wave, and storm  
342 surge model for southern Louisiana and Mississippi. part ii: Synoptic  
343 description and analysis of hurricanes Katrina and Rita. *Monthly Weather  
Review*, 138(2):378–404.
- 345 Dietrich, J., Westerink, J., Kennedy, A., Smith, J., Jensen, R., Zijlema, M.,  
346 Holthuijsen, L., Dawson, C., Luettich, R., Powell, M., et al. (2011).  
347 Hurricane Gustav (2008) waves and storm surge: Hindcast, synoptic  
348 analysis, and validation in southern Louisiana. *Monthly Weather Review*,  
349 139(8):2488–2522.
- 350 Dobbelaere, T., Muller, E., Gramer, L., Holstein, D., and Hanert, E. (2020a).  
351 Report on the potential origin of the SCTLD in the Florida Reef Tract.  
352 Available online at: [https://floridadep.gov/rcp/coral/documents/  
353 report-potential-origin-sctld-florida-reef-tract](https://floridadep.gov/rcp/coral/documents/report-potential-origin-sctld-florida-reef-tract).
- 354 Dobbelaere, T., Muller, E. M., Gramer, L. J., Holstein, D. M., and Hanert, E.  
355 (2020b). Coupled epidemi-hydrodynamic modeling to understand the  
356 spread of a deadly coral disease in Florida. *Frontiers in Marine Science*,  
357 7:1016.
- 358 Donelan, M., Haus, B., Reul, N., Plant, W., Stiassnie, M., Gruber, H., Brown,  
359 O., and Saltzman, E. (2004). On the limiting aerodynamic roughness of  
360 the ocean in very strong winds. *Geophysical Research Letters*, 31(18).
- 361 Figueiredo, J., Baird, A. H., and Connolly, S. R. (2013). Synthesizing larval  
362 competence dynamics and reef-scale retention reveals a high potential  
363 for self-recruitment in corals. *Ecology*, 94(3):650–659.
- 364 Frys, C., Saint-Amand, A., Le Hénaff, M., Figueiredo, J., Kuba, A., Walker, B.,  
365 Lambrechts, J., Vallaeyns, V., Vincent, D., and Hanert, E. (2020). Fine-  
366 scale coral connectivity pathways in the Florida Reef Tract: implications  
367 for conservation and restoration. *Frontiers in Marine Science*, 7:312.
- 368 Garcia-Pineda, O., Androulidakis, Y., Le Hénaff, M., Kourafalou, V., Hole,  
369 L. R., Kang, H., Staples, G., Ramirez, E., and DiPinto, L. (2020). Mea-  
370 suring oil residence time with GPS-drifters, satellites, and Unmanned  
371 Aerial Systems (UAS). *Marine pollution bulletin*, 150:110644.

- 372 Geuzaine, C. and Remacle, J.-F. (2009). Gmsh: A 3-d finite element mesh  
373 generator with built-in pre-and post-processing facilities. *International*  
374 *journal for numerical methods in engineering*, 79(11):1309–1331.
- 375 Harper, B., Kepert, J., and Ginger, J. (2010). *Guidelines for converting*  
376 *between various wind averaging periods in tropical cyclone conditions*.  
377 Citeseer.
- 378 Hegermiller, C. A., Warner, J. C., Olabarrieta, M., and Sherwood, C. R.  
379 (2019). Wave–current interaction between Hurricane Matthew wave  
380 fields and the Gulf Stream. *Journal of Physical Oceanography*,  
381 49(11):2883–2900.
- 382 Hoffmeister, J. and Multer, H. (1968). Geology and origin of the Florida Keys.  
383 *Geological Society of America Bulletin*, 79(11):1487–1502.
- 384 Holthuijsen, L. H., Powell, M. D., and Pietrzak, J. D. (2012). Wind and waves  
385 in extreme hurricanes. *Journal of Geophysical Research: Oceans*,  
386 117(C9).
- 387 Janssen, P. A. (1991). Quasi-linear theory of wind-wave generation applied  
388 to wave forecasting. *Journal of physical oceanography*, 21(11):1631–  
389 1642.
- 390 Johns, W. E. and Schott, F. (1987). Meandering and transport variations  
391 of the Florida Current. *Journal of physical oceanography*, 17(8):1128–  
392 1147.
- 393 Knaff, J. A., Sampson, C. R., and Musgrave, K. D. (2018). Statistical tropi-  
394 cal cyclone wind radii prediction using climatology and persistence:  
395 Updates for the western North Pacific. *Weather and Forecasting*,  
396 33(4):1093–1098.
- 397 Knutson, T. R., McBride, J. L., Chan, J., Emanuel, K., Holland, G., Landsea,  
398 C., Held, I., Kossin, J. P., Srivastava, A., and Sugi, M. (2010). Tropical  
399 cyclones and climate change. *Nature geoscience*, 3(3):157–163.
- 400 Komen, G., Hasselmann, S., and Hasselmann, K. (1984). On the exis-  
401 tence of a fully developed wind-sea spectrum. *Journal of physical*  
402 *oceanography*, 14(8):1271–1285.

- 403 Kourafalou, V. H. and Kang, H. (2012). Florida Current meandering and  
404 evolution of cyclonic eddies along the Florida Keys Reef Tract: Are they  
405 interconnected? *Journal of Geophysical Research: Oceans*, 117(C5).
- 406 Kundu, P. K. (1976). Ekman veering observed near the ocean bottom.  
407 *Journal of Physical Oceanography*, 6(2):238–242.
- 408 Landsea, C. W. and Franklin, J. L. (2013). Atlantic hurricane database un-  
409 certainty and presentation of a new database format. *Monthly Weather  
410 Review*, 141(10):3576–3592.
- 411 Lee, T. N., Leaman, K., Williams, E., Berger, T., and Atkinson, L. (1995).  
412 Florida Current meanders and gyre formation in the southern Straits  
413 of Florida. *Journal of Geophysical Research: Oceans*, 100(C5):8607–  
414 8620.
- 415 Lee, T. N. and Mayer, D. A. (1977). Low-frequency current variability and  
416 spin-off eddies along the shelf off southeast Florida. *Collected Reprints*,  
417 1(1):344.
- 418 Lee, T. N. and Smith, N. (2002). Volume transport variability through the  
419 Florida Keys tidal channels. *Continental Shelf Research*, 22(9):1361–  
420 1377.
- 421 Lee, T. N. and Williams, E. (1988). Wind-forced transport fluctuations of the  
422 Florida Current. *Journal of Physical Oceanography*, 18(7):937–946.
- 423 Li, Z. and Johns, B. (1998). A three-dimensional numerical model of surface  
424 waves in the surf zone and longshore current generation over a plane  
425 beach. *Estuarine, Coastal and Shelf Science*, 47(4):395–413.
- 426 Lidz, B. H. and Shinn, E. A. (1991). Paleoshorelines, reefs, and a rising sea:  
427 South florida, usa. *Journal of Coastal Research*, pages 203–229.
- 428 Lin, N. and Chavas, D. (2012). On hurricane parametric wind and appli-  
429 cations in storm surge modeling. *Journal of Geophysical Research:  
430 Atmospheres*, 117(D9).
- 431 Liu, Y. and Weisberg, R. H. (2012). Seasonal variability on the West Florida  
432 shelf. *Progress in Oceanography*, 104:80–98.

- 433 Liu, Y., Weisberg, R. H., and Zheng, L. (2020). Impacts of hurricane Irma  
434 on the circulation and transport in Florida Bay and the Charlotte Harbor  
435 estuary. *Estuaries and Coasts*, 43(5):1194–1216.
- 436 Liubartseva, S., Coppini, G., Lecci, R., and Clementi, E. (2018). Tracking  
437 plastics in the Mediterranean: 2D Lagrangian model. *Marine pollution  
438 bulletin*, 129(1):151–162.
- 439 Longuet-Higgins, M. S. (1970). Longshore currents generated by obliquely  
440 incident sea waves. *Journal of geophysical research*, 75(33):6778–  
441 6789.
- 442 Longuet-Higgins, M. S. and Stewart, R. (1964). Radiation stresses in water  
443 waves; a physical discussion, with applications. In *Deep sea research and oceanographic abstracts*, volume 11, pages 529–562. Elsevier.
- 445 Madsen, O. S., Poon, Y.-K., and Gruber, H. C. (1989). Spectral wave  
446 attenuation by bottom friction: Theory. In *Coastal Engineering 1988*,  
447 pages 492–504.
- 448 Malmstadt, J., Scheitlin, K., and Elsner, J. (2009). Florida hurricanes and  
449 damage costs. *southeastern geographer*, 49(2):108–131.
- 450 Marsooli, R., Lin, N., Emanuel, K., and Feng, K. (2019). Climate change  
451 exacerbates hurricane flood hazards along US Atlantic and Gulf Coasts  
452 in spatially varying patterns. *Nature communications*, 10(1):1–9.
- 453 Mei, C. C. (1989). *The applied dynamics of ocean surface waves*, volume 1.  
454 World scientific.
- 455 Moon, I.-J., Ginis, I., Hara, T., and Thomas, B. (2007). A physics-based  
456 parameterization of air–sea momentum flux at high wind speeds and  
457 its impact on hurricane intensity predictions. *Monthly weather review*,  
458 135(8):2869–2878.
- 459 Pinelli, J.-P., Roueche, D., Kijewski-Correa, T., Plaz, F., Prevatt, D., Zisis,  
460 I., Elawady, A., Haan, F., Pei, S., Gurley, K., et al. (2018). Overview  
461 of damage observed in regional construction during the passage of  
462 Hurricane Irma over the State of Florida. In *Forensic Engineering 2018: Forging Forensic Frontiers*, pages 1028–1038. American Society of  
463 Civil Engineers Reston, VA.

- 465 Powell, M. D., Houston, S. H., Amat, L. R., and Morisseau-Leroy, N. (1998).  
466      The HRD real-time hurricane wind analysis system. *Journal of Wind*  
467      *Engineering and Industrial Aerodynamics*, 77:53–64.
- 468 Powell, M. D., Vickery, P. J., and Reinhold, T. A. (2003). Reduced drag coeffi-  
469      cient for high wind speeds in tropical cyclones. *Nature*, 422(6929):279–  
470      283.
- 471 Schott, F. A., Lee, T. N., and Zantopp, R. (1988). Variability of structure and  
472      transport of the Florida Current in the period range of days to seasonal.  
473      *Journal of Physical Oceanography*, 18(9):1209–1230.
- 474 Shinn, E. A. (1988). The geology of the Florida Keys. *Oceanus*, 31(1):46–53.
- 475 Siadatmousavi, S. M., Jose, F., and Stone, G. (2011). Evaluation of two WAM  
476      white capping parameterizations using parallel unstructured SWAN  
477      with application to the Northern Gulf of Mexico, USA. *Applied Ocean*  
478      *Research*, 33(1):23–30.
- 479 Sikirić, M. D., Roland, A., Janeković, I., Tomazić, I., and Kuzmić, M. (2013).  
480      Coupling of the Regional Ocean Modeling System (roms) and Wind  
481      Wave Model. *Ocean Modelling*, 72:59–73.
- 482 Smith, N. P. (1982). Response of Florida Atlantic shelf waters to hurricane  
483      David. *Journal of Geophysical Research: Oceans*, 87(C3):2007–2016.
- 484 Tolman, H. L. et al. (2009). User manual and system documentation of  
485      WAVEWATCH III TM version 3.14. *Technical note, MMAB Contribution*,  
486      276:220.
- 487 Van Den Bremer, T. and Breivik, Ø. (2018). Stokes drift. *Philosophical Trans-*  
488      *actions of the Royal Society A: Mathematical, Physical and Engineering*  
489      *Sciences*, 376(2111):20170104.
- 490 Villas Bôas, A. B., Cornuelle, B. D., Mazloff, M. R., Gille, S. T., and Arduin,  
491      F. (2020). Wave–current interactions at meso-and submesoscales:  
492      Insights from idealized numerical simulations. *Journal of Physical*  
493      *Oceanography*, 50(12):3483–3500.
- 494 Weisberg, R., Liu, Y., and Mayer, D. (2009). Mean circulation on the west  
495      Florida continental shelf observed with long-term moorings. *Geophys.*  
496      *Res. Lett.*, 36:L19610.

- 497 Weisberg, R. H. and Zheng, L. (2006). Hurricane storm surge simulations  
498 for Tampa Bay. *Estuaries and Coasts*, 29(6):899–913.
- 499 Wu, L., Chen, C., Guo, P., Shi, M., Qi, J., and Ge, J. (2011). A FVCOM-  
500 based unstructured grid wave, current, sediment transport model, I.  
501 Model description and validation. *Journal of Ocean University of China*,  
502 10(1):1–8.
- 503 Xian, S., Feng, K., Lin, N., Marsooli, R., Chavas, D., Chen, J., and Hatzikyri-  
504 akou, A. (2018). Brief communication: Rapid assessment of damaged  
505 residential buildings in the Florida Keys after Hurricane Irma. *Natural  
506 Hazards and Earth System Sciences*, 18(7):2041–2045.
- 507 Zhang, C., Durgan, S. D., and Lagomasino, D. (2019). Modeling risk of man-  
508 groves to tropical cyclones: A case study of Hurricane Irma. *Estuarine,  
509 Coastal and Shelf Science*, 224:108–116.